Research Article

Nano Research
2023, 16(7): 9352–9363

ISSN 1998-0124 CN 11-5974/O4
https://doi.org/10.1007/s12274-023-5569-2

Selective Pb^{2+} removal and electrochemical regeneration of fresh and recycled FeOOH

Lei Wang[1,2], Lexane Deligniere[1,2], Samantha Husmann[1], Regina Leiner[3], Carsten Bahr[4], Shengjie Zhang[5], Chaochao Dun[6], Matthew M. Montemore[5], Markus Gallei[3,7], Jeffrey J. Urban[6], Choonsoo Kim[8,9], and Volker Presser[1,2,7] (✉)

[1] *INM—Leibniz Institute for New Materials, Campus D2 2, Saarbrücken 66123, Germany*
[2] *Department of Materials Science and Engineering, Saarland University, Campus D2 2, Saarbrücken 66123, Germany*
[3] *Polymer Chemistry, Saarland University, Campus C4 2, Saarbrücken 66123, Germany*
[4] *GEH Wasserchemie GmbH & Co. KG, Adolf-Köhne-Straße 4, Osnabrück 49090, Germany*
[5] *Department of Chemical and Biomolecular Engineering, Tulane University, New Orleans, LA 70118, USA*
[6] *The Molecular Foundry, Lawrence Berkeley National Laboratory Berkeley, Berkeley, CA 94720, USA*
[7] *Saarene–Saarland Center for Energy Materials and Sustainability, Campus C4 2, Saarbrücken 66123, Germany*
[8] *Department of Environmental Engineering with Institute of Energy/Environment Convergence Technologies, Kongju National University, 1223-24 Cheonan-daero, Cheonan-si 31080, Republic of Korea*
[9] *Department of Future Convergence Engineering, Kongju National University, 1223-24 Cheonan-daero, Cheonan-si 31080, Republic of Korea*

Received: 31 October 2022 / **Revised:** 1 February 2023 / **Accepted:** 9 February 2023

ABSTRACT

Heavy metal pollution is a key environmental problem. Selectively extracting heavy metals could accomplish water purification and resource recycling simultaneously. Adsorption is a promising approach with a facile process, adaptability for the broad concentration of feed water, and high selectivity. However, the adsorption method faces challenges in synthesizing high-performance sorbents and regenerating adsorbents effectively. FeOOH is an environmentally friendly sorbent with low-cost production on a large scale. Nevertheless, the selectivity behavior and regeneration of FeOOH are seldom studied. Therefore, we investigated the selectivity of FeOOH in a mixed solution of Co^{2+}, Ni^{2+}, and Pb^{2+} and proposed to enhance the capacity of FeOOH and regenerate it by using external charges. Without charge, the FeOOH electrode shows a Pb^{2+} uptake capacity of 20 mg/g. After applying a voltage of −0.2/+0.8 V, the uptake capacity increases to a maximum of 42 mg/g and the desorption ratio is 70%–80%. In 35 cycles, FeOOH shows a superior selectivity towards Pb^{2+} compared with Co^{2+} and Ni^{2+}, with a purity of 97% ± 3% in the extracts. The high selectivity is attributed to the lower activation energy for Pb^{2+} sorption. The capacity retentions at the 5th and the 35th cycles are ca. 80% and ca. 50%, respectively, comparable to the chemical regeneration method. With industrially exhausted granular ferric hydroxide as the electrode material, the system exhibits a Pb^{2+} uptake capacity of 37.4 mg/g with high selectivity. Our work demonstrates the feasibility of regenerating FeOOH by charge and provides a new approach for recycling and upcycling FeOOH sorbent.

KEYWORDS

FeOOH, electrochemical regeneration, selective separation, heavy metal ions

1 Introduction

With rapid industrialization, a large number of heavy metals are released into the aquatic environment, which are prominently toxic and carcinogenic [1]. In particular, Pb causes serious physiological harm as Pb^{2+}, such as cardiovascular diseases, anemia, loss of taste and smell, growth impairment, and even kidney failure [2, 3]. Separating and recovering metal ions from water could simultaneously accomplish water regimentation and resource recovery [4]. Several methods, such as electrodeposition [5], ion exchange [6], shear-induced dissociation coupling with ultrafiltration [7], and adsorption [8] can be used to separate Pb^{2+} from water. Among these methods, adsorption has gained continuous attention and has been considered promising for Pb^{2+} separation due to its simple operation, high efficiency, and flexibility for different types of wastewater [8, 9].

Sorption methods usually accomplish selectivity via two paths: modification with specific functional groups or spatial size effects [10]. Some functional groups prefer to chelate or complex Pb^{2+} over other cations [11]. For instance, Wang et al. utilized sodium alginate solution to remove Pb^{2+}, Cu^{2+}, and Cd^{2+} from wastewater selectively [12]. The sodium alginate contains –COO^- and –OH groups, which are considered hard bases in general. These functional groups prefer to remove Pb^{2+} (intermediate acid) rather than Cu^{2+} (intermediate acid) and Cd^{2+} (soft acid) [13]. Polymers using functional monomers (e.g., acrylic acid) or special crosslinkers (like tetraethoxysilane) can be synthesized with specific metal ions as templates via ion imprinting technology.

Address correspondence to volker.presser@leibniz-inm.de

Consequently, the well-ordered functional group and the cavity with fixed size and shape exhibit selectivity towards the templated heavy metals [14]. For example, Zhang et al. studied the selectivity performance of a magnetic ion-imprinted polymer (Fe_3O_4@SiO_2@IIP) in a mixed solution of 10 μg/L Pb^{2+}, 10 μg/L Cu^{2+}, 10 μg/L Cd^{2+}, 10 μg/L Zn^{2+}, and 10 μg/L Hg^{2+}. The material could selectively remove Pb^{2+} with selectivity factors of 6.02 (Pb^{2+}/Cu^{2+}), 8.29 (Pb^{2+}/Zn^{2+}), 3.31 (Pb^{2+}/Cd^{2+}), and 7.41 (Pb^{2+}/Zn^{2+}). In contrast, the non-imprinted polymer does not preferentially remove Pb^{2+} [15]. Ge et al. prepared poly(acrylic acid) grafted and glutaraldehyde-crosslinked chitosan using Pb^{2+} as a template ion. In that work, the uptake capacity of Pb^{2+} is at least 2.5 times that of Cu^{2+}, Hg^{2+}, Cd^{2+}, Co^{2+}, or Zn^{2+} [16].

FeOOH is a promising sorbent to remove heavy metals from water due to its easy preparation, non-toxicity, low cost, and high selectivity [17, 18]. Xu et al. studied the sorption behavior of FeOOH towards Cd, Cu, and Pb from water. The maximum Pb^{2+} uptake capacity is 99.5 mg/g at pH = 6, while the maximum Cd^{2+} sorption capacity is only 12.4 mg/g. Rahimi and co-workers utilized nano α-FeOOH and nano γ-FeOOH to remove Pb^{2+}. The thermodynamic maximum adsorption capacities of α-FeOOH and γ-FeOOH are 820 and 528 mg/g, respectively [19]. Pranudat et al. synthesized a hybrid of granular ferric hydroxide (GFH) [20] and an acid gel cation exchanger to recover Pb^{2+} from lead-acid battery wastewater [21]. The adsorbent could recover ca. 60% Pb^{2+} at pH = 5 in the first cycle; the recovery ratio decreases to 40% in the fourth cycle. So far, few studies have investigated the selective Pb^{2+} removal performance of FeOOH and the post-treatment of spent FeOOH sorbent. Generally, there are two approaches to treat FeOOH sorbents: directly abandoning them (afterward treated as hazardous waste) and regenerating them with chemicals (Fig. 1) [22]. The former does not lead to sustainable development, while the latter requires chemical treatment. Additionally, the reusability of FeOOH sorbents has remained unclear since previous studies only examined the reusability under a limited cycle number (mostly less than 5 cycles) [23].

In this work, we enhanced the sorption capacity of FeOOH and demonstrated an effective way to regenerate the material by applying an electrical potential. This approach to sorbent regeneration eliminates the need for undesirable chemical treatment. The adsorption and selectivity performance (without charge) of FeOOH was first studied in a mixed solution containing Pb^{2+}, Co^{2+}, and Ni^{2+}. The mechanism was analyzed via *ex-situ* X-ray photoelectron spectroscopy (XPS) and density functional theory (DFT) calculations. Subsequently, we investigated the uptake capacity and regeneration performance of the FeOOH electrode for 35 cycles under an electric field. Assisted by charge, the FeOOH electrode shows higher uptake capacity and superior selectivity towards Pb^{2+}, with the regeneration ratio reaching as high as 70%–80%. In addition, the selectivity of FeOOH towards Pb^{2+} was investigated in a solution with a larger number of competing ions and a higher concentration ratio between competing ions and Pb^{2+}. With this approach, we also explored the possibility of upcycling the exhausted GFH adsorbent from the industry.

2 Materials and methods

2.1 FeOOH electrode preparation

The FeOOH electrode was prepared by mixing commercial FeOOH powder (< 0.3 mm, GEH Wasserchemie GmbH & Co. KG), acetylene carbon (Alfa Aesar, 99.5%), and polytetrafluoroethylene binder (60 wt.% dispersion in water, Sigma Aldrich) with a mass ratio of 8:1:1 in ethanol. The mixture was ground to gain a homogeneous paste. Subsequently, the paste was rolled to 100 or 200 μm free-standing electrodes by the rolling cylinder press (MTI HR01, MTI Corp), and the electrodes were dried at 40 °C under vacuum overnight. The exhausted-FeOOH (E-FeOOH) electrode was made with the same procedure but with abandoned-GFH (A-GFH). A-GFH was obtained from a drinking water treatment plant located in the Eifel region in the south of North Rhine-Westphalia, Germany, where GFH (produced by GEH Wasserchemie GmbH & Co. KG) is applied as the adsorbent to remove Pb^{2+} from drinking water. The treatment plant consists of an adsorption filter with a bed volume (BV) of 1.8 m^3 (= 2.1 t GFH). A total of 56,000 m^3 of water is treated in the

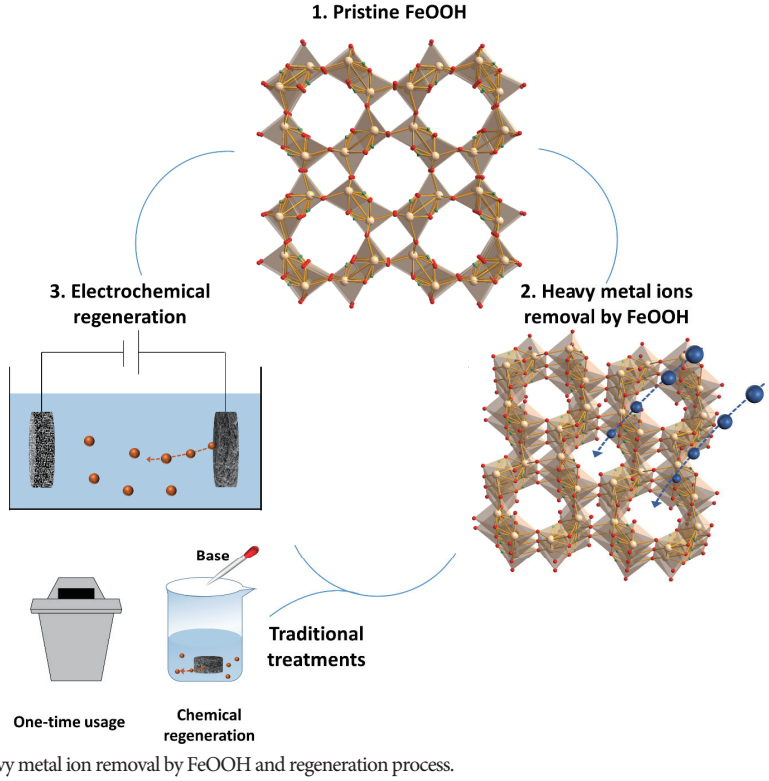

Figure 1 Schematic image of heavy metal ion removal by FeOOH and regeneration process.

plant over 1 year. The components of GFH before and after treating the drinking water are shown in Table S1 in the Electronic Supplementary Material (ESM).

2.2 Electrochemical measurements

The electrochemical measurements were accomplished in a custom-built cell [24]. In this three-electrode system, the FeOOH electrode (diameter of 12 mm and mass loading of 841 ± 37 mg/cm^3) and carbon cloth (Kynol 509-20, diameter of 12 mm), separated by a glass fiber mat (diameter of 13 mm, GF/A, Whatman), served as the working electrode and the counter electrode, respectively; Ag/AgCl (3 M NaCl) was used as the reference electrode. Cyclic voltammetry (CV) and galvanostatic charge/discharge with the potential limitation (GCPL) measurements were conducted with a VSP300 potentiostat (Bio-Logic). The cell was scanned from −0.3 to +0.6 V vs. Ag/AgCl with a rate of 1 mV/s to obtain cyclic voltammograms. For GCPL, the cell was charged/discharged with a cutoff potential of −0.3 and +0.6 V vs. Ag/AgCl with a specific current of 0.1 A/g. The electrolytes for CV and GCPL measurements were 10 mM $Pb(NO_3)_2$, 10 mM $Co(NO_3)_2$, 10 mM $Ni(NO_3)_2$, or a mixed solution (10 mM $Pb(NO_3)_2$, 10 mM $Co(NO_3)_2$, and 10 mM $Ni(NO_3)_2$). The pH of all the solutions was 4.

2.3 Sorption experiments

The adsorption kinetics of FeOOH was investigated by adding 65 mg FeOOH powder in a 15 mL single cation solution containing 10 mM $Pb(NO_3)_2$, 10 mM $Co(NO_3)_2$, or 10 mM $Ni(NO_3)_2$, and in a 15 mL mixed solution with the concentration of 10 mM for each cation (Pb^{2+}, Co^{2+}, and Ni^{2+}). The pH of all the solutions was 4. The solutions with various treatment times were shaken by a roller mixer (RM 5W-40, CAT) with a speed of 36 rpm at 25 °C. After 10, 20, and 40 min, 1, 2, 3, and 20 h, the samples were taken out and filtered by the glass fiber membrane filter (pore size 1.0 μm, Whatman) to remove the sorbent powders. Adsorption experiments of FeOOH in single-cation solution were also conducted at 40 and 50 °C to study the effect of temperature on the kinetics. At higher temperature, the samples were treated for shortened treatment times, that were, 5, 10, 20, and 40 min, 1, 2, 3, and 7 h. All other conditions were the same as the experiment at 25 °C.

To investigate the influence of pH on Pb^{2+} sorption, 65 mg FeOOH powder was added in 10 mM $Pb(NO_3)_2$ solution (15 mL) over the pH range from 2 to 6. The adsorption time was 20 h to reach equilibrium. The isothermal adsorption experiments were conducted in a series of $Pb(NO_3)_2$ solutions (0.1–10 mM) with a pH of 4 at 25 °C. The other conditions were the same as the kinetic experiment. The concentration of all cations was measured by inductively coupled plasma-optical emission spectroscopy (ICP-OES, ARCOS FHX22, SPECTRO Analytical Instruments). The same operation was adopted for the control group except for adding sorbents in all the adsorption experiments.

2.4 Electrochemical-assisted adsorption and desorption experiments

Electrochemical-assisted adsorption and desorption experiments were conducted in a common electrochemical cell. Briefly, the cell was composed of a working electrode (FeOOH electrode or E-FeOOH electrode), a counter electrode (carbon cloth, Kynol 509-20), and a water channel filled with a glass fiber mat (GF/A, Whatman). The counter electrode was separated from the water channel by an anion exchange membrane (FAS-PET-130, Fumatech) to eliminate the influence of the counter electrode on cation uptake and release. A mixture of 10 mM $Pb(NO_3)_2$, 10 mM $Co(NO_3)_2$, and 10 mM $Ni(NO_3)_2$ or the electrolyte with more competing ions (10 mM Pb^{2+}, 10 mM Co^{2+}, 10 mM Ni^{2+}, 100 mM Na^+, 100 mM K^+, 100 mM Mg^{2+}, and 100 mM Ca^{2+}) was used as the feed water. The recovery solution was 10 mM NaCl or 10 mM LiCl (for the experiment with more competing ions). Both feed water and recovery solution circulated from and back to the reservoir with a flow rate of 5 mL/min. Two operations were conducted with the cell. First, the cell was left to rest for 24 h with feed water flowing in the cell. Afterward, the Milli-Q water flushed into the cell to reduce the residual feed water, and the electrolyte then switched to the recovery solution. The cell was charged to 0.8 V with a specific current of 0.1 A/g and then held at this cell voltage for 1 h. The second operation was the same as the first one, except that the cell was discharged to −0.2 V with a specific current of 0.1 A/g and then held at this cell voltage for 2 h to extract cations. The second operation was used to explore the performance of FeOOH under applied potential. Before and after the discharge/charge process, we took samples from the reservoir to measure the concentration by ICP-OES. After took out the sample, the feed water reservoir was refilled to maintain a constant volume. In contrast, no more water was added to the volume of the recovery tank (except for the experiment for 200 μm FeOOH electrode). The details are shown in Table S2 in the ESM.

2.5 Material characterization

Scanning electron microscopy (SEM) was carried out using a ZEISS Gemini 500 system at acceleration voltages of 1–3 kV. The powder or electrode samples were attached to an aluminum stub with conductive carbon tape. No sputtering was performed prior to analysis. Energy-dispersive X-ray (EDX) spectra were obtained using X-Max Silicon Detector (Oxford Instruments) attached as a column to the SEM instrument at 15 kV. Transmission electron microscopy (TEM) measurement was accomplished at an electron beam energy of 200 kV, using JEOL 2100-F equipped with an Oxford high solid-angle silicon drift detector, EDX, and a high-angle annular dark field (HAADF) detector. The crystal structure of FeOOH was analyzed via the X-ray diffraction (XRD, D8 Advanced diffractometer, Bruker AXS) equipped with a copper X-ray source (40 kV, 40 mA). We used a Renishaw InVia instrument equipped with an Nd:YAG laser to obtain the Raman spectra. The spectra were scanned under a laser wavelength of 532 nm, with a laser spot of about 2 μm and a power exposure of 0.5 mW. The spectral resolution was 1.2 cm^{-1}. The Raman system was calibrated with single-crystalline silicon. XPS results were obtained from a Thermo Fisher XPS system with a monochromatized Al-Kα line ($h\nu$ = 1486.6 eV) as the photon source. The spectra were acquired at a spot size of 400 μm and constant pass energy. Charge neutralization was accomplished via a combined low-energy electron/ion flood source. The zeta potential of FeOOH was measured in 0.1 M $NaNO_3$ with various pH values ranging from 3 to 10 by a Zetasizer Nano-series instrument (Malvern Instruments, UK). Before the measurement, the mixture was ultrasonicated for 15 s to obtain the dispersion of FeOOH.

2.6 DFT calculations

All calculations in this work were performed using spin-polarized DFT with the generalized gradient approximation-Perdew–Burke–Ernzerhof (GGA-PBE) functional [25]. To correctly calculate the localized Fe 3d electrons, the Dudarev [26] rotationally invariant approach was employed to DFT + U calculations. The effective Hubbard U parameter (U_{eff}) that equals the difference between the effective on-site Coulomb parameter (U) and exchange parameter (J) was set to 5 eV, that is, $U_{eff} = U - J = 5$ eV, which has been widely used and has been proved to be consistent with the experimental studies of FeOOH [27–29]. A 400 eV cutoff energy and a 7 × 12 × 7 Monkhorst–Pack k-point

mesh [30] were used for bulk calculations, and a 7 × 12 × 1 mesh was used for surface relaxation. All calculations were performed with the Vienna *ab initio* simulation package (VASP) [31]. The structures were visualized by the Visualization for Electronic and STructural Analysis (VESTA) [32].

In bulk calculations, a unit cell contained 16 Fe atoms (2 stacked 8-membered rings), and all atoms and the unit cell were relaxed. In surface calculations, 16 or 24 Fe atoms were in a unit cell with the bottom half fixed during relaxation. The adsorption energy, or reaction energy, is calculated as $E = E_{M(II)FeOOH} + E_{H2O} - E_{M(II)H2O} - E_{FeOOH}$, where $E_{M(II)H2O}$ is the energy of metal ions with four water molecules (M = Pb^{2+}, Co^{2+}, or Ni^{2+}), E_{FeOOH} is the energy of a clean bulk/surface, E_{H2O} is the energy of four water molecules, and $E_{M(II)FeOOH}$ is the energy of a bulk or surface where two H^+ are substituted by a metal ion. Under this convention, a more negative number indicates stronger adsorption.

2.7 Calculations

The average domain size of FeOOH was calculated according to the Scherrer equation

$$\tau = \frac{K\lambda}{\beta \cos\theta} \quad (1)$$

where τ is the mean domain size of FeOOH, K is the dimensionless shape factor with the typical value of 0.9, λ is the X-ray wavelength of copper, that is, 0.1564 nm, β is the line broadening at half the maximum intensity (rad), and θ is the Bragg angle (rad). β and θ were obtained from the cumulative fit peak. The line-broadening induced by the system was corrected using a corundum standard.

The cation adsorption capacity at time t (Q_t) was calculated according to Eq. (2)

$$Q_t = \frac{(c_0 - c) \times V}{m} \quad (2)$$

where c_0 and c are the concentrations before and after treatment, respectively, V is the volume of the solution, and m is the mass of the sorbent.

The kinetics was simulated according to Eq. (3) (pseudo-first-order (PFO)) and Eq. (4) (pseudo-second-order (PSO))

$$Q_t = Q_e\left(1 - e^{-k_1 t}\right) \quad (3)$$

$$Q_t = \frac{k_2 Q_e^2 t}{1 + k_2 Q_e t} \quad (4)$$

where Q_e (mg/g) is the equilibrium adsorption capacity, k_1 (min^{-1}) and k_2 (g·min/mg) are the constants, representing the adsorption rates for the pseudo-first-order model and pseudo-second-order model, respectively.

The activation energy was calculated via the Arrhenius equation

$$k = Ae^{\frac{-E_a}{RT}} \quad (5)$$

where k is the rate constant, A is the pre-exponential factor, E_a is the activation energy, R is the universal gas constant, and T is the temperature.

In the adsorption isotherm experiment, the data were fitted according to Langmuir (Eq. (6)) and Freundlich (Eq. (7)) isothermal models

$$Q_e = \frac{K_L Q_{max} C_e}{1 + K_L C_e} \quad (6)$$

$$Q_e = K_F C_e^{1/n} \quad (7)$$

where Q_{max} is the maximum sorption capacity, C_e is the equilibrium concentration, K_L and K_F are the Langmuir constant and Freundlich constant, respectively, and n is the heterogeneity factor.

The uptake/release capacity and capacity regeneration ratio were calculated according to Eqs. (8) and (9), respectively

$$\text{Cation uptake/release capacity} = \frac{|c - c_0| \times V}{m} \quad (8)$$

$$\text{Capacity regeneration ratio} = \frac{\text{Cation release capacity}}{\text{Cation uptake capacity}} \times 100\% \quad (9)$$

The selectivity of FeOOH was evaluated via the purity of Pb in the extracts, calculated according to Eq. (10)

$$\text{Purity of Pb in the extracts} = \frac{\Delta c_{pb}}{\Delta c_{all}} \times 100\% \quad (10)$$

where Δc_{pb} and Δc_{all} are the concentration changes of Pb^{2+} and all the cations in the recovery solution, respectively.

To explore the energy efficiency of this method, we calculated the charge efficiency and energy consumption according to Eqs. (11) and (12), respectively

$$\text{Charge efficiency} = \frac{Pb^{2+}\text{release capacity} \times F}{Q \times M} \times 100\% \quad (11)$$

where F is the Faraday constant, 96,485 C/mol, Q is the charge transferred during the charging process, and M is the molar mass of Pb.

$$\text{Energy consumption} = \frac{E_{electrical}}{Pb^{2+}\text{release capacity}} \quad (12)$$

where $E_{electrical}$ is the consumed electrical energy during one cycle.

3 Results and discussion

3.1 Characterization of FeOOH

Figure 2(a) shows the scanning electron micrograph of FeOOH particles, showing an agglomerated bulky form due to the interaction of OH inside FeOOH particles [19]. Each FeOOH grain is rod-like, with a length of around 20 nm and a width of about 4 nm, as shown by the TEM image (Fig. 2(b)). The *d*-spacing of 0.26 nm shown by the high-resolution TEM (HR-TEM) image represents the (211) crystal plane of FeOOH (PDF 34-1266). Figure 2(c) shows the XRD pattern of FeOOH. As can be seen, the XRD pattern is broad, fitting with standard pattern of β-FeOOH (PDF 34-1266), which implies that commercial FeOOH powder has poor crystallinity. The reflections at 17.5°, 26.8°, 35.5°, 39.6°, 43.4°, 46.8°, and 56.4° are assigned to the (200), (310), (211), (301), (510), (411), and (521) crystal planes, respectively. The broad peak at around 63° could result from the overlap of the reflections of β-FeOOH higher than 60°. The average domain size of the commercial FeOOH is around 6 nm, calculated according to the Scherrer equation (Eq. (1)). To further determine the phase of FeOOH, we conducted Raman measurements (Fig. 2(d)). The four apparent bands at 312, 397, 525, and 727 cm^{-1} are the diagnostic bands for identifying β-FeOOH, consistent with results in previous work [33]. The bands at 312 and 397 cm^{-1} correspond to the Fe–O vibrational mode of octahedral Fe sites [34]. Moreover, the bands at 525 and 727 cm^{-1} are assigned to asymmetric Fe–OH bending mode [35].

3.2 The sorption performance of FeOOH

We investigated the sorption capacity of FeOOH by immersing the powder in a single-cation solution (10 mM $Pb(NO_3)_2$, 10 mM

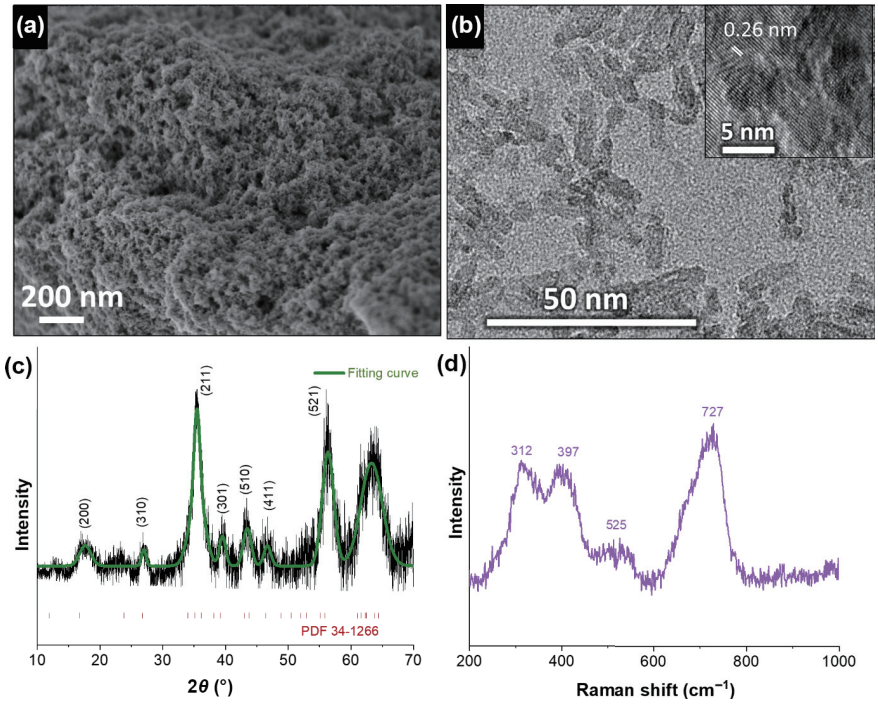

Figure 2 (a) SEM image, (b) TEM image (the inset is an HR-TEM image), (c) XRD pattern and fitting curve, and (d) Raman spectrum of iron hydroxide powder.

$Co(NO_3)_2$, or 10 mM $Ni(NO_3)_2$). Since the pH of the mixed solution (10 mM Pb^{2+}, 10 mM Ni^{2+}, and 10 mM Co^{2+}) is close to 4, and the Pb^{2+} adsorption capacity does not significantly improve when changing the pH from 4 to 6 (Fig. S1 in the ESM), we keep the pH equal to 4 in all the experiments. Figure 3(a) shows the sorption capacity of FeOOH at various treatment times in the Pb^{2+} solution. The adsorption kinetics was analyzed under pseudo-first-order (Eq. (3)) and pseudo-second-order (Eq. (4)) models. The correlation coefficients (R^2) of the PFO model and PSO model are 0.97 and 0.99, respectively; this indicates that the PSO model is more suitable to describe the sorption kinetics of FeOOH, suggesting the main sorption process of Pb^{2+} on FeOOH is monolayer and chemical sorption. According to the PSO model, the simulated equilibrium capacity is 40.7 ± 0.7 mg/g. The maximum Pb^{2+} sorption capacity is 42.2 ± 3.7 mg/g, obtained by fitting the data with the Langmuir isotherm model (Fig. S2 in the ESM). The data are comparable to other works reporting the performance of other adsorbents at pH = 4 [36–38]. HAADF and EDX measurements reveal that the absorbed Pb^{2+} ions are uniformly distributed on/in the FeOOH (Fig. S3 in the ESM). Similarly, the PSO model also fits better than the PFO model when $Co(NO_3)_2$ or $Ni(NO_3)_2$ serves as the feed water (Figs. 3(b) and 3(c)). On the contrary, the Co^{2+}-sorption and Ni^{2+}-sorption capacities (3.7 ± 0.1 and 3.6 ± 0.1 mg, respectively) are much lower than the Pb^{2+}-sorption capacity. To further demonstrate that FeOOH has better selectivity towards Pb^{2+}, we tested the performance of FeOOH in a mixed solution of 10 mM Pb^{2+}, 10 mM Co^{2+}, and 10 mM Ni^{2+}. Figure 3(d) shows the additive inverse of the concentration change at various adsorption times. The concentration of Pb^{2+} decreases as the adsorption time rises, and reaches equilibrium after around 180 min treatment. The measured concentration changes of Co^{2+} and Ni^{2+} are lower than the standard derivation due to the low sorption capacities of Co^{2+} and Ni^{2+}. The simulated equilibrium capacity utilizing the PSO model is 41.1 ± 0.9 mg/g (Fig. 3(e)).

To investigate the sorption mechanism, we further conducted *ex-situ* XPS of the sorbents before and after immersing them in various solutions for 24 h at 25 °C (Fig. 4 and Fig. S4 in the ESM). All the data were calibrated using adventitious carbon. Compared with the initial FeOOH, there is an obvious Pb 4f spectrum in the XPS spectrum of FeOOH after immersing in the $Pb(NO_3)_2$ (Fig. 4(a)). Figure 4(b) shows the Pb 4f spectra of the FeOOH sorbent after soaking in $Pb(NO_3)_2$ solution. The peaks at 137.8, 138.2, and 139.2 eV are assigned to the binding energies of Pb $4f_{7/2}$ in PbO, $Pb(OH)_2$, and $Pb(NO_3)_2$, respectively (according to the NIST Standard Reference Database 2). The peak area at 138.2 eV is much higher than that at 137.8 eV, implying that Pb^{2+} mainly exists in the form of FeOHPb^{2+} and some forms the complex with the O of FeOOH by replacing the protons [39, 40]. After sorbing Pb^{2+}, the chemical surroundings of O and Fe also changed, reflected in the +0.1 eV shift of hydroxide bond (O–H) in FeOOH (Fig. 4(c)) and −0.2 eV shift of Fe^{3+} $2p_{3/2}$ (Fig. 4(d)). Additionally, the zeta potential measurement indicates that the process is not electrostatic sorption due to the positive potential of FeOOH at pH = 4 (Fig. S5 in the ESM). β-FeOOH crystalized in the tetragonal *I*4/*m* space group. Fe atoms are octahedrally surrounded by six O/OH, and the linked octahedra form double strings parallel to the *c*-axis. The double strings share a corner with neighboring double strings, forming a tunnel structure (Fig. S6 in the ESM) [41]. To investigate the Pb^{2+} sorption position in/on FeOOH, we used DFT to calculate the reaction energy of Pb^{2+} sorption at three possible positions: in bulk (tunnel) (Fig. 5(a)), on the (100) surface (cutting the bulk parallel to the *b*-*c* plane) (Fig. 5(b)), and on the (010) surface (cutting the bulk parallel to the *a*-*c* plane) (Fig. 5(c)). The reaction energy in the tunnel is −3.13 eV, less negative than on the surfaces (Fig. 5(d)), suggesting the adsorption in the tunnel is less thermodynamically favorable than on the surface. This may be because the confined space in the tunnel (the distance between two non-adjacent H atoms of 3.6–3.8 Å, close to the ionic diameter of Pb, Fig. S7 in the ESM) would produce steric hindrance, requiring more energy to insert in tunnels. Compared with adsorption on the (010) surface (−4.87 eV), Pb^{2+} is more thermodynamically stable when adsorbed on the (100) surface (−5.31 eV). This is likely due to both less steric hindrance and more active O atoms that are less coordinated in the (100) surface (Fig. 5(b)).

Different from the results of FeOOH for Pb^{2+} sorption, we could not obtain reasonable Ni 2p nor Co 2p spectrum by measuring the FeOOH sample after Co^{2+} or Ni^{2+} sorption, corresponding to the slight changes of the binding energies of O 1s and Fe 2p (Figs.

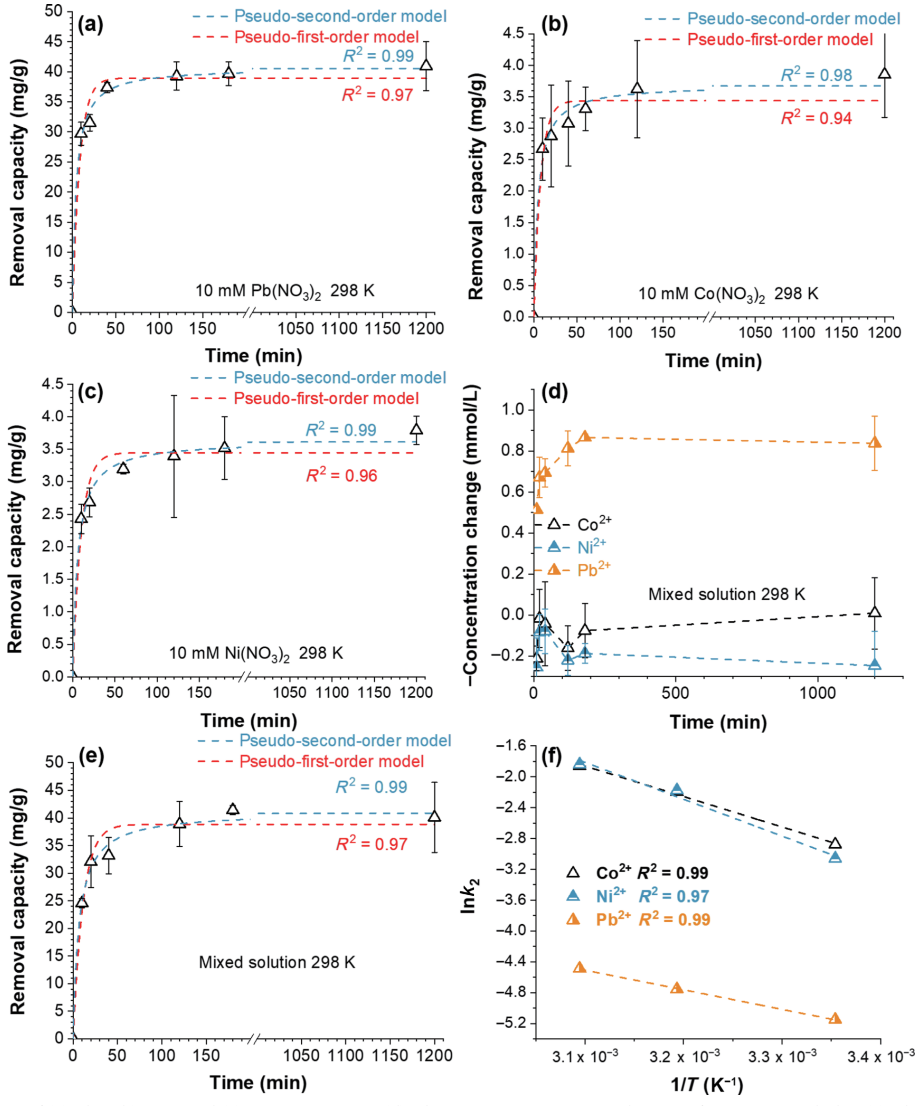

Figure 3 Sorption kinetics of (a) Pb^{2+}, (b) Co^{2+}, and (c) Ni^{2+} on FeOOH. (d) The minus concentration changes of Co^{2+}, Ni^{2+}, and Pb^{2+}. (e) The removal capacity of Pb^{2+} after the adsorption in mixed solution for different times. (f) Sorption thermodynamics of Co^{2+}, Ni^{2+}, and Pb^{2+} by FeOOH.

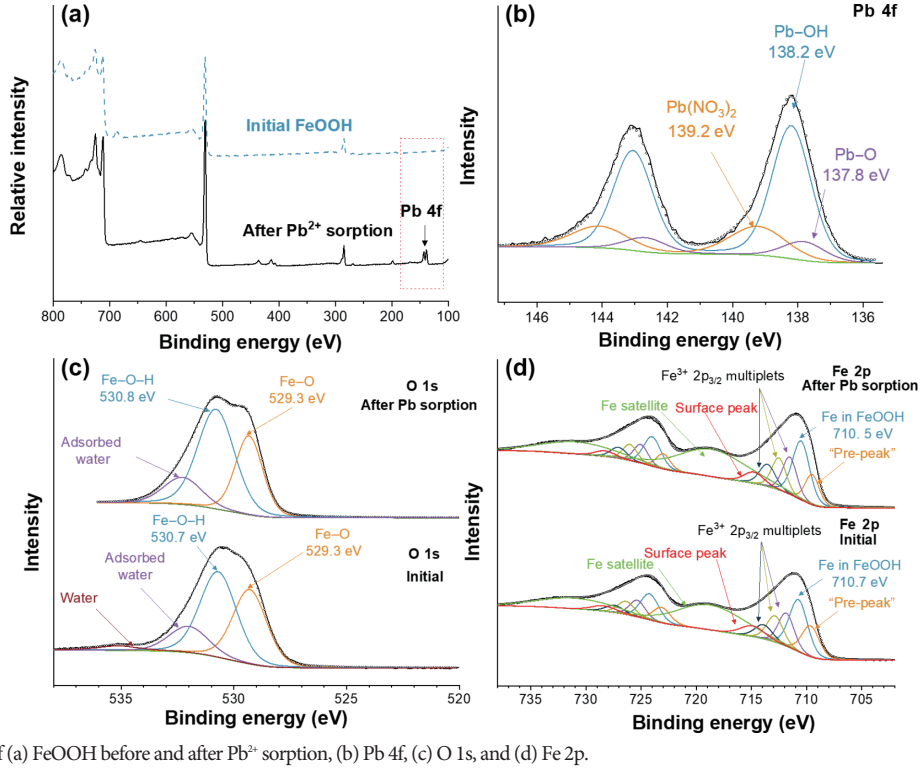

Figure 4 XPS spectra of (a) FeOOH before and after Pb^{2+} sorption, (b) Pb 4f, (c) O 1s, and (d) Fe 2p.

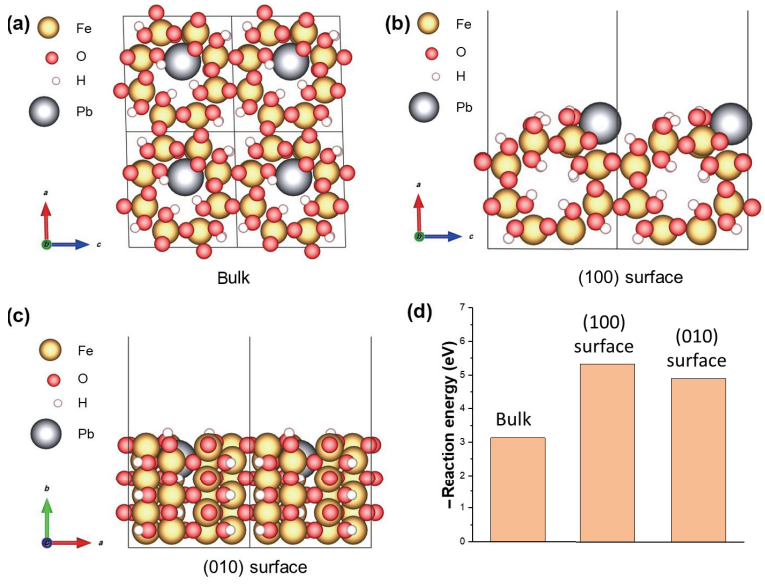

Figure 5 Calculated optimized structures of FeOOH for Pb^{2+} sorption at various places: (a) in bulk, (b) on the (100) surface, and (c) on the (010) surface. (d) The corresponding reaction energy for Pb^{2+} adsorption at different places.

S4(a) and S4(b) in the ESM). The sorbent treating the mixed solution does not display reasonable Ni 2p nor Co 2p spectrum. In contrast, the Pb 4f spectra are similar to the sorbents soaked in a single Pb^{2+} solution; this result is due to high selectivity towards Pb^{2+} (Fig. S4(c) in the ESM) [37]. To explore the reasons for the affinity for Pb^{2+}, we performed kinetic sorption experiments at various temperatures (Fig. S8 in the ESM) and calculated the activation energy according to the Arrhenius equation (Eq. (5)). As shown in Fig. 3(f), the value of $\ln k_2$ shows a good linear relationship with $1/T$, implying the fitting is reliable. The activation energy of Pb^{2+} is 21.1 ± 0.6 kJ/mol, much less than that of Ni^{2+} (39.7 ± 4.7 kJ/mol) and Co^{2+} (32.7 ± 1.8 kJ/mol). This means that the sorption of Pb^{2+} is kinetically more favorable than Co^{2+} and Ni^{2+}. This result is consistent with the order of the covalent index, which is generally used to assess the affinity between adsorbent ligands and metal ions among Pb^{2+}, Co^{2+}, and Ni^{2+} (Pb^{2+} > Co^{2+} > Ni^{2+}) [42]. Generally, the larger the covalent index, the easier the coordination between adsorbent and metal ions. Analogous to Pb^{2+}, DFT calculations predict that both Co^{2+} and Ni^{2+} adsorb more strongly on the (100) surface (−4.51 and −5.16 eV, respectively, Figs. S9(a) and S9(b) in the ESM) than on the (010) surface (−4.46 and −5.10 eV, respectively, Figs. S9(c) and S9(d) in the ESM). This indicates that the (100) surface is the most favorable sorption site. The DFT results also indicate that Pb^{2+} adsorbs more favorably on the (100) surface than Ni^{2+} or Co^{2+}, which agrees with the selective sorption of Pb^{2+} in our experiments.

3.3 Electrochemical-assisted adsorption and desorption

We first studied the electrochemical properties of FeOOH with a three-electrode system in the mixed electrolyte (10 mM $Pb(NO_3)_2$, 10 mM $Co(NO_3)_2$, and 10 mM $Ni(NO_3)_2$). There are no deposition peaks of any heavy metals with the cutoff potential ranging between −0.3 and +0.6 V vs. Ag/AgCl (Fig. S10(a) in the ESM). The capacitance of the 121 μm thick electrode is 3.5 times that of the 220 μm electrode (7 vs. 2 F/g), as shown in Fig. S10(b) in the ESM. This phenomenon is due to longer diffusion path and higher internal resistance of thicker electrode [43]. Afterward, we investigated the electrochemical performance of the 121 μm electrode in the single-cation solution. In the single-cation solution, there is a pair of redox peaks occurring in the range between −0.3 and 0.6 V vs. Ag/AgCl (Fig. S10(c) in the ESM); the specific peak current is not high (5.6 mA/g in $Pb(NO_3)_2$, 6.7 mA/g in $Ni(NO_3)_2$, and 8.7 mA/g in $Co(NO_3)_2$), which implies the charge involved in the redox reaction is small. The GCPL curves with no obvious plateau also manifest this (Fig. S10(e) in the ESM). To explore the reason for the redox peaks, we conducted CV measurements in 10 mM $NaNO_3$ and NaCl. The pH of both these electrolytes is 7. As can be seen, obvious redox peaks occur in the $NaNO_3$ electrolyte, indicating that the redox peaks are not because of the proton (Fig. S10(d) in the ESM). In contrast, a pair of broad and slight redox peaks occur within the NaCl electrolyte, indicating that the redox peaks are related to NO_3^-. Different anions interact differently with the β-FeOOH structure, following a trend similar to the Hofmeister series. Stronger interactions cause lattice distortions due to the incorporation of the anion in the structure. Very weak interactions are observed for NO_3^-, meaning that the structure remains essentially the same. In a less distorted structure, the tunnels along the *b*-axis allow for better ion diffusion and, thus, a sharper redox process [44]. The formal potential of the redox reactions depends on the concentration of NO_3^-. As the concentration increases, the formal potential shifts positively. A redox peak also appears in the mixed solution when the potential window extends to 0.8 V vs. Ag/AgCl (Fig. S10(d) in the ESM). FeOOH has different capacities in different electrolytes. The capacity in the mixed electrolyte is the highest, with 2.24 ± 0.16 mAh/g in the first cycle, because this electrolyte has the lowest resistance (Fig. S10(f) in the ESM). In the single-cation solution, FeOOH shows the highest capacity in the $Pb(NO_3)_2$ electrolyte, with 1.23 ± 0.2 mAh/g, which is 1.5 times and 2.7 times as much as the capacities in the $Co(NO_3)_2$ and $Ni(NO_3)_2$ electrolytes, respectively.

Afterward, we explored the performance of FeOOH under an electric field. Figure 6(a) shows the concentration changes of all the cations in 35 cycles. During the discharge process, the concentration change of Pb^{2+} is always negative, implying that the Pb^{2+} is immobilized in the electrode. In contrast, the concentration changes of Co^{2+} and Ni^{2+} are close to 0 and less than the standard derivation due to the low uptake capacities of Co^{2+} and Ni^{2+}. From the *ex-situ* EDX spectrum, we could not find Co^{2+} nor Ni^{2+} on the electrode either due to the trace amounts of Co^{2+} and Ni^{2+} stored in the electrode (Fig. S11 in the ESM). During the charging operation, the Pb^{2+} ions are released from the FeOOH, manifesting in the positive concentration change of Pb^{2+}. The concentration changes of Co^{2+} and Ni^{2+} are also positive but much less than that of Pb^{2+}. The purity of Pb^{2+} in the total extracts in each cycle is

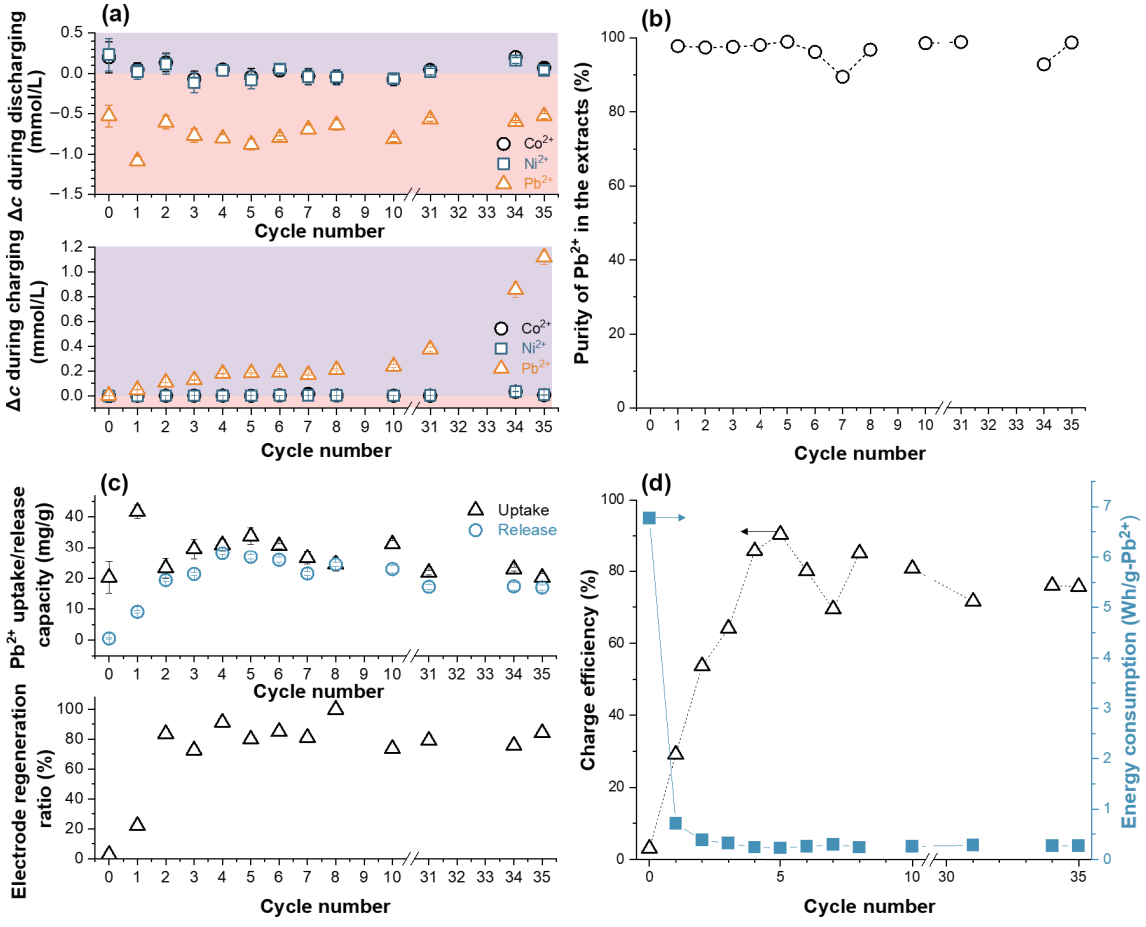

Figure 6 The electrochemical experiments with an electrode with a thickness of 121 μm in a mixed solution of 10 mM Co^{2+}, 10 mM Ni^{2+}, and 10 mM Pb^{2+}: (a) concentration changes of Co^{2+}, Ni^{2+}, and Pb^{2+} during the discharging (upper) and charging (bottom) processes at different cycles; (b) the purity of Pb^{2+} in the extracts; (c) the uptake/release capacity of Pb^{2+} (upper) and capacity regeneration percentage (bottom) at different cycles; and (d) the charge efficiency and energy consumption at different cycles.

above 90% with an average of 96.8% ± 2.7%, demonstrating that FeOOH has an affinity for Pb^{2+} (Fig. 6(b)). The electrode with a thickness of 220 μm exhibits similar results with an average purity of Pb^{2+} in the total extracts of 93.7% ± 4.5% (Fig. S12(a) in the ESM). FeOOH exhibits better selectivity towards Pb^{2+} than the reported materials, where the purity of Pb^{2+} in the adsorbed ions is generally lower than 80% (Table 1). The high selectivity indicates that apart from the adsorption process, the ions removed by charge also show selectivity towards Pb^{2+}, which may be because of the lower dehydration energy of Pb^{2+}, compared with Co^{2+} and Ni^{2+} (Fig. S13 in the ESM) [45]. Considering the complex component of actual industrial wastewater, we also investigated the selectivity performance of FeOOH electrodes in the feed water containing common alkali and alkaline metal earth ions (Na^{+}, K^{+}, Ca^{2+}, and Mg^{2+}) with higher concentrations. Figure S14 in the ESM shows the ratio of each element in the extracts. The purity of Pb^{2+} is higher than 60% (except for the first cycle), with an average of 62.9%, indicating the system still shows selectivity towards Pb^{2+} even though competing ions exist in 10-fold higher concentrations. Na^{+} is the predominant impurity in the extracts; the ratios of K^{+}, Ca^{2+}, and Mg^{2+} over all cations are similar. Co^{2+} and Ni^{2+} are the lowest components in the extracts (lower than 1%).

Figure 6(c) shows the uptake/release capacity of FeOOH. In the 0^{th} cycle (i.e., the first operation), the uptake capacity is 20.2 mg/g after 24 h adsorption. This value is lower than the adsorption capacity of FeOOH powder because the electrode is denser and has less contact area. The release capacity in the 0^{th} cycle is only 0.54 mg/g, with a regeneration ratio of 2.7%. This low value is because the ions require more time to migrate into the inner pores of the electrode. As the electrode goes through several charging/discharging processes, the capacity regeneration ratio of the electrode increases to 70%–80%, with an uptake capacity of 25–30 mg/g (Fig. 6(c)). The uptake capacity retention at the 5^{th} cycle is ~ 80%. Furthermore, after 35 cycles, the uptake capacity remains 20.2 mg/g, like the adsorption capacity without charge and 50% of the uptake capacity of the first cycle. To investigate the contribution ratios of the sorption and charge to the uptake capacity after 35 cycles, we flushed the cell with the electrolyte without discharging for 2 h. The Pb-removal capacity is 9.1 mg/g, indicating the Pb removal performance is enhanced by 120%, benefiting from the charge. This regeneration performance is comparable to the FeOOH absorbent regenerated by chemicals (capacity retention of 70%–80% after 5 cycles) [22]. The capacity fading is due to the Fe loss. The concentration of Fe after 35 cycles in the feed water is 0.14 ± 0.001 mM. The charge efficiency in the 35 cycles is higher than 70% except for the first four cycles (the electrode activation period), as shown in Fig. 6(d). Figure 6(d) also displays the energy consumption of the system. In the 0^{th} cycle, the energy consumption is much higher than that of other cycles due to the low release capacity in this cycle. The average consumption is 0.31 ± 0.12 Wh/g-Pb^{2+} (excluding the 0^{th} cycle). The FeOOH with a thickness of 220 μm shows similar results with a relatively lower capacity of 20–25 mg/g (Fig. S12(b) in the ESM) and a regeneration ratio of 40%–60% (Fig. S12(c) in the ESM). Additionally, the energy efficiency is lower, with a charge efficiency of 49.3% ± 12.6% and a consumption of 0.44 ± 0.11 Wh/g-Pb^{2+} (Fig. S12(d) in the ESM). The worse performance is due to the higher resistance of the thicker electrodes [43].

Table 1 Selectivity performance of some sorbents for Pb^{2+} adsorption

Material	Mechanism	Solution (mg/L)	Capacity (mg/g)	Purity of Pb^{2+} in the extracts (%)	References
Nano-sized silica functionalized with diethanolamine	Sorption	Pb^{2+}, Zn^{2+}, Cu^{2+}, Pd^{2+}, Ge^{4+}, Al^{3+}, Co^{2+}, Cd^{2+}, As^{3+}, Mg^{2+}, and Sb^{3+}, 100 mg/L of each cation	90.3	24.3	[46]
Bimetallic coordination polymer	Sorption	Pb^{2+}, 20 Zn^{2+}, 13.9 Ni^{2+}, 14.6 Cd^{2+}, 18 Ca^{2+}, 22.1 Mg^{2+}, 18.1	19.2	72.5	[47]
Poly(pyrrole methane)	Sorption	Pb^{2+}, 100 Ni^{2+}, 100	~ 28	97.9	[10]
Bael leaves	Sorption	Pb^{2+}, 9.76 Mn^{2+}, 9.25 Ni^{2+}, 10.9 Cd^{2+}, 9.36 Zn^{2+}, 9.64 Mg^{2+}, 9.6 Fe^{2+}, 8.17 Cu^{2+}, 10.36	—	59.7	[48]
Crosslinked N,O-carboxymethyl-chitosan resin with Pb(II) as template ions	Sorption	Pb^{2+}, 4144 Cu^{2+}, 1280 Zn^{2+}, 1300	431.0	53.7	[49]
FeOOH	**Electrochemistry**	**Pb^{2+}, 2072 Co^{2+}, 589 Ni^{2+}, 589**	**1st cycle, 42.0 35th cycle, 20.2**	**96.8**	**This work**

Post-mortem analysis of the electrodes after cycling was carried out with SEM, XRD, Raman, and XPS measurements to investigate whether the structure change or water scouring caused the Fe loss. We observed some cracks on the electrode after 35 cycles, while there are almost no cracks on the initial electrode (Fig. S15 in the ESM). Compared with the initial powder, the Raman spectrum (Fig. S16(a) in the ESM) and XRD pattern (Fig. S16(b) in the ESM) of the electrode after 35 cycles do not change except that the diffraction pattern becomes much sharper and narrower, meaning the crystalline degree of the material increases. Compared with the initial electrode, the binding energy of Fe^{3+} $2p_{3/2}$ shifts by −0.1 eV, indicating the Fe valence does not change significantly (Fig. S16(c) in the ESM). The Fe loss is mainly due to mechanical damage (e.g., water scouring).

The work so far has demonstrated the performance and properties of fresh FeOOH. While the latter is cost-attractive, it is even more environmentally attractive to reuse FeOOH that is already used for its initial target application in a sewage facility. In principle, the chemical application of FeOOH should not prevent its use as an electrochemically regeneratable Pb-removal electrode. Thus, we also explored GFH material that was used to treat the drinking water in the south of North Rhine-Westphalia, Germany. After treatment, A-GFH must be disposed in accordance with waste guidelines, that is, usually deposited in a hazardous waste landfill without any recycling treatment or second-life perspective. A-GFH is granular with the size of hundred micrometers and adsorbed Pb^{2+} on the surface (Figs. S17(a) and S17(b) in the ESM). Compared with the pristine FeOOH powder, A-GFH has the same XRD pattern except for the reflection at 17.5° (Fig. S17(c) in the ESM), which may due to the initial difference between GFH and fine FeOOH powder. When the cell is flushed with the feed water for 24 h without applying an electric potential, the concentration of Pb^{2+} in the feed water changes only slightly (0.02 ± 0.08 mM). This shows that the material has reached its chemical sorption limit and cannot uptake any more Pb^{2+} via chemisorption (Fig. 7(a)). From the 1st to the 10th cycle, the concentration changes of Pb^{2+}, Co^{2+}, and Ni^{2+} are similar to the results of the FeOOH electrode (Fig. 7(a)). This indicates the E-FeOOH also has high selectivity towards Pb^{2+} with a purity of 96.1% ± 2.3%. The Pb^{2+} uptake capacity is 37.4 ± 2.4 mg/g in the first ten cycles, with a capacity regeneration above 70% (except for the 1st cycle), as shown in Fig. 7(c). The average energy consumption is 0.31 ± 0.28 Wh/g-Pb^{2+}(Fig. 7(d)), close to that of fresh FeOOH electrode. The results indicate that the spent GFH sorbent could be recycled by utilizing charges. This could drastically reduce the amount of waste GFH and open up perspectives towards upcycling and circularity.

4 Conclusions

In this work, we used the FeOOH sorbent to selectively remove Pb^{2+} and regenerated it via the electrochemical method. We explored the sorption performance in 10 mM $Pb(NO_3)_2$, 10 mM $Co(NO_3)_2$, 10 mM $Ni(NO_3)_2$, or a mixed solution of Pb^{2+}, Co^{2+}, and Ni^{2+}. In both single-cation and mixed solutions, the adsorption kinetics fits better with the pseudo-second-order model. In the single-cation solution, the equilibrium sorption capacity of Pb^{2+} is 40.7 ± 0.7 mg/g, much higher than the Co^{2+}- and Ni^{2+}-sorption capacities. In the mixed solution, the Pb^{2+}-sorption capacity still reaches 38.7 ± 0.7 mg/g. The affinity for Pb^{2+} is attributed to a higher covalent index of Pb^{2+} and a lower activation energy for the sorption. Under the electric field, the FeOOH also exhibits good selectivity towards Pb^{2+} in the feed water containing 10 mM $Pb(NO_3)_2$, 10 mM $Co(NO_3)_2$, and 10 mM $Ni(NO_3)_2$, with a purity of 96.8% ± 2.7% in the extracts, meaning that both adsorption and electrochemical processes prefer Pb^{2+} due to its high electronegativity and low dehydration energy. FeOOH also exhibits good selectivity towards Pb^{2+} (62.9% purity in the extracts) in the feed water containing more cations with higher concentrations than Pb^{2+}. Utilizing the charge, 70%–80% of the Pb^{2+} could be released from the electrode in every cycle (except the first two cycles). Consequently, the capacity remains 20.2 mg/g at the 35th cycle, enhanced by 120% compared with capacity without charge. The capacity at the 35th cycle is half that in the first cycle; the regeneration ratio is comparable to the method using chemicals with the benefits of being time and cost-effective with less environmental impact. The exhausted GFH also manifests a Pb^{2+} uptake capacity of 37.4 mg/g under the charge filed. Our work provides a new avenue for regenerating FeOOH sorbent.

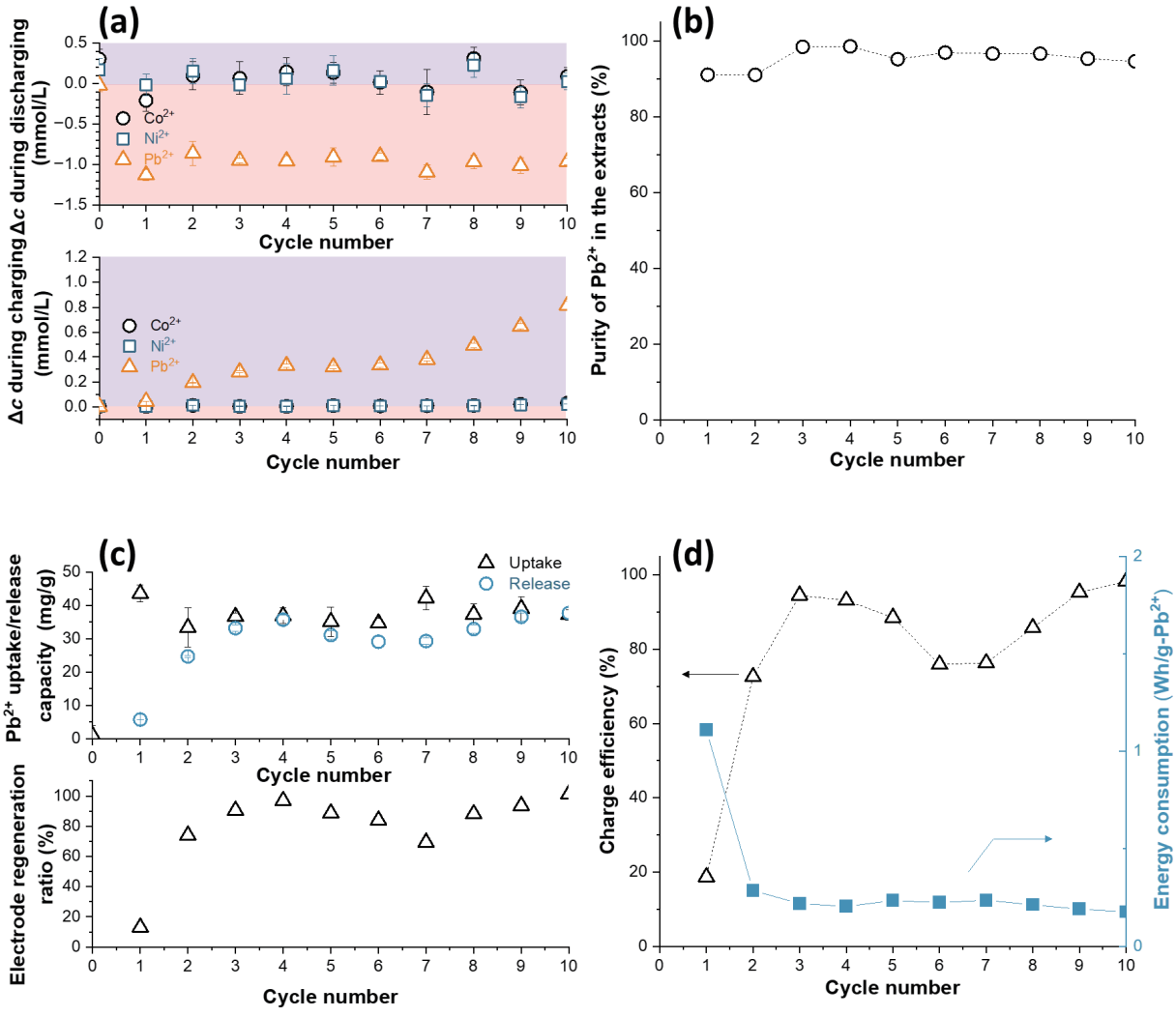

Figure 7 The electrochemical experiments with an electrode made by exhausted GFH in a mixed solution of 10 mM Co^{2+}, 10 mM Ni^{2+}, and 10 mM Pb^{2+}: (a) concentration changes of Co^{2+}, Ni^{2+}, and Pb^{2+} during the discharging (upper) and charging (bottom) processes at different cycles; (b) the purity of Pb^{2+} in the extracts; (c) the uptake/release capacity of Pb^{2+} (upper) and capacity regeneration percentage (bottom) at different cycles; and (d) the charge efficiency and energy consumption at different cycles.

Acknowledgments

L. W. acknowledges funding from the Chinese Scholarship Council (CSC, No. 201906260277). The work of L. D. was part of the École Européenne d'Ingénieurs en Génie des Matériaux (EEIGM) carried out at Saarland University. Work at the Molecular Foundry was supported by the Office of Science, Office of Basic Energy Sciences, of the U.S. Department of Energy (No. DE-AC02-05CH11231). We acknowledge support for the eLiRec project by the European Union from the European Regional Development Fund (EFRE) and the State of Saarland, Germany. S. J. Z. acknowledges support from Tulane University.

Funding note: Open Access funding enabled and organized by Pr ojekt DEAL.

Electronic Supplementary Material: Supplementary material (the sorption capacity of FeOOH powder in 10 mM $Pb(NO_3)_2$ with various pH values; adsorption isotherms of Pb^{2+} by FeOOH, HADDF-STEM image and EDX mappings of FeOOH sorbent after immersing in $Pb(NO_3)_2$ solution, XPS spectra of FeOOH sorbent after immersing in $Ni(NO_3)_2$, $Co(NO_3)_2$, and mixed solution, zeta potential of FeOOH powder, sorption kinetics of Co^{2+}, Ni^{2+}, and Pb^{2+} by FeOOH at 313 and 323 K, crystal structure of FeOOH, CV and galvanostatic charge/discharge profiles of FeOOH electrode with different thicknesses in the mixed solution, CV and galvanostatic charge/discharge results of 121 μm FeOOH electrode measured in various electrolytes, the discharge capacity of 121 μm FeOOH during 100 cycles in different electrolytes, DFT calculation results of Co^{2+} and Ni^{2+} sorption on the surface created by cleaving the lattice along the (100) and (010) surfaces, SEM image and EDX mappings of FeOOH electrode at discharge state, electrochemical performance of 220 μm FeOOH in the mixed solution, theoretical diameter and dehydration energy of Co^{2+}, Ni^{2+}, and Pb^{2+}, the ratio of each element in the extracts in the experiment conducted in the feed water containing 10 mM Pb^{2+}, 10 mM Co^{2+}, 10 mM Ni^{2+}, 100 mM Na^{+}, 100 mM K^{+}, 100 mM Mg^{2+}, and 100 mM Ca^{2+}, SEM images of initial FeOOH electrode and electrode after 35 cycles, post-mortem Raman, XRD, and Raman results of FeOOH electrode after 35 cycles, SEM, EDX, and XRD results of exhausted GFH, element compositions of GFH before and after water treatment, and experimental details using FeOOH and exhausted GFH electrodes) is available in the online version of this article at https://doi.org/10.1007/s12274-023-5569-2.

References

[1] Afonne, O. J.; Ifediba, E. C. Heavy metals risks in plant foods—Need to step up precautionary measures. *Curr. Opin. Toxicol.* **2020**, *22*, 1–6.

[2] Jaishankar, M.; Tseten, T.; Anbalagan, N.; Mathew, B. B.; Beeregowda, K. N. Toxicity, mechanism, and health effects of some heavy metals. *Interdiscip. Toxicol.* **2014**, *7*, 60–72.

[3] Singh, R.; Gautam, N.; Mishra, A.; Gupta, R. Heavy metals and living systems: An overview. *Indian J. Pharmacol.* **2011**, *43*, 246–253.

[4] Chen, R.; Feng, J. Y.; Jeon, J.; Sheehan, T.; Rüttiger, C.; Gallei, M.; Shukla, D.; Su, X. Structure and potential-dependent selectivity in redox-metallopolymers: Electrochemically mediated multicomponent metal separations. *Adv. Funct. Mater.* **2021**, *31*, 2009307.

[5] Doulakas, L.; Novy, K.; Stucki, S.; Comninellis, C. Recovery of Cu, Pb, Cd, and Zn from synthetic mixture by selective electrodeposition in chloride solution. *Electrochim. Acta* **2000**, *46*, 349–356.

[6] Nekouei, R. K.; Pahlevani, F.; Assefi, M.; Maroufi, S.; Sahajwalla, V. Selective isolation of heavy metals from spent electronic waste solution by macroporous ion-exchange resins. *J. Hazard. Mater.* **2019**, *371*, 389–396.

[7] Le, H. S.; Qiu, Y. R. Selective separation of Cd(II), Zn(II), and Pb(II) from Pb-Zn smelter wastewater via shear induced dissociation coupling with ultrafiltration. *Korean J. Chem. Eng.* **2020**, *37*, 784–791.

[8] Ali, J.; Wang, H. B.; Ifthikar, J.; Khan, A.; Wang, T.; Zhan, K.; Shahzad, A.; Chen, Z. L.; Chen, Z. Q. Efficient, stable, and selective adsorption of heavy metals by thio-functionalized layered double hydroxide in diverse types of water. *Chem. Eng. J.* **2018**, *332*, 387–397.

[9] Zhou, X.; Jin, C.; Liu, G. F.; Wu, G. M.; Huo, S. P.; Kong, Z. W. Functionalized lignin-based magnetic adsorbents with tunable structure for the efficient and selective removal of Pb(II) from aqueous solution. *Chem. Eng. J.* **2021**, *420*, 130409.

[10] Liu, Y. P.; Zhang, W. L.; Zhao, C. C.; Wang, H.; Chen, J.; Yang, L.; Feng, J. T.; Yan, W. Study on the synthesis of poly(pyrrole methane)s with the hydroxyl in different substituent position and their selective adsorption for Pb^{2+}. *Chem. Eng. J.* **2019**, *361*, 528–537.

[11] Idris, S. A.; Harvey, S. R.; Gibson, L. T. Selective extraction of mercury(II) from water samples using mercapto functionalised-MCM-41 and regeneration of the sorbent using microwave digestion. *J. Hazard. Mater.* **2011**, *193*, 171–176.

[12] Wang, F.; Lu, X. W.; Li, X. Y. Selective removals of heavy metals (Pb^{2+}, Cu^{2+}, and Cd^{2+}) from wastewater by gelation with alginate for effective metal recovery. *J. Hazard. Mater.* **2016**, *308*, 75–83.

[13] Li, J.; Xie, L. X.; Guo, R.; Wang, H.; Liang, Z. P.; Yao, H. Q.; Ma, S. L. Facile preparation of Fe_3O_4/MoS_4 for ultra fast and highly selective uptake towards Hg^{2+}, Pb^{2+}, and Ag^{+}. *J. Alloys Compd.* **2020**, *823*, 153819.

[14] Chen, A. H.; Yang, C. Y.; Chen, C. Y.; Chen, C. Y.; Chen, C. W. The chemically crosslinked metal-complexed chitosans for comparative adsorptions of Cu(II), Zn(II), Ni(II), and Pb(II) ions in aqueous medium. *J. Hazard. Mater.* **2009**, *163*, 1068–1075.

[15] Zhang, M. L.; Zhang, Z. H.; Liu, Y. N.; Yang, X.; Luo, L. J.; Chen, J. T.; Yao, S. Z. Preparation of core–shell magnetic ion-imprinted polymer for selective extraction of Pb(II) from environmental samples. *Chem. Eng. J.* **2011**, *178*, 443–450.

[16] Ge, H. C.; Hua, T. T.; Chen, X. D. Selective adsorption of lead on grafted and crosslinked chitosan nanoparticles prepared by using Pb^{2+} as template. *J. Hazard. Mater.* **2016**, *308*, 225–232.

[17] Li, H.; Li, W.; Zhang, Y. J.; Wang, T. S.; Wang, B.; Xu, W.; Jiang, L.; Song, W. G.; Shu, C. Y.; Wang, C. R. Chrysanthemum-like α-FeOOH microspheres produced by a simple green method and their outstanding ability in heavy metal ion removal. *J. Mater. Chem.* **2011**, *21*, 7878–7881.

[18] Wang, B.; Wu, H. B.; Yu, L.; Xu, R.; Lim, T. T.; Lou, X. W. Template-free formation of uniform urchin-like α-FeOOH hollow spheres with superior capability for water treatment. *Adv. Mater.* **2012**, *24*, 1111–1116.

[19] Rahimi, S.; Moattari, R. M.; Rajabi, L.; Derakhshan, A. A.; Keyhani, M. Iron oxide/hydroxide (α, γ-FeOOH) nanoparticles as high potential adsorbents for lead removal from polluted aquatic media. *J. Ind. Eng. Chem.* **2015**, *23*, 33–43.

[20] Walsh, K.; Mayer, S.; Rehmann, D.; Hofmann, T.; Glas, K. Equilibrium data and its analysis with the Freundlich model in the adsorption of arsenic(V) on granular ferric hydroxide. *Sep. Purif. Technol.* **2020**, *243*, 116704.

[21] Pranudta, A.; Chanthapon, N.; Kidkhunthod, P.; El-Moselhy, M. M.; Nguyen, T. T.; Padungthon, S. Selective removal of Pb from lead-acid battery wastewater using hybrid gel cation exchanger loaded with hydrated iron oxide nanoparticles: Fabrication, characterization, and pilot-scale validation. *J. Environ. Chem. Eng.* **2021**, *9*, 106282.

[22] Wang, S. D.; Lan, H. C.; Liu, H. J.; Qu, J. H. Fabrication of FeOOH hollow microboxes for purification of heavy metal-contaminated water. *Phys. Chem. Chem. Phys.* **2016**, *18*, 9437–9445.

[23] Liu, Y. B.; Yang, S. N.; Jiang, H. L.; Yang, B.; Fang, X. F.; Shen, C. S.; Yang, J. M.; Sand, W.; Li, F. Sea urchin-like FeOOH functionalized electrochemical CNT filter for one-step arsenite decontamination. *J. Hazard. Mater.* **2021**, *407*, 124384.

[24] Aslan, M.; Zeiger, M.; Jäckel, N.; Grobelsek, I.; Weingarth, D.; Presser, V. Improved capacitive deionization performance of mixed hydrophobic/hydrophilic activated carbon electrodes. *J. Phys. Condens. Matter* **2016**, *28*, 114003.

[25] Perdew, J. P.; Burke, K.; Ernzerhof, M. Generalized gradient approximation made simple. *Phys. Rev. Lett.* **1996**, *77*, 3865–3868.

[26] Dudarev, S. L.; Botton, G. A.; Savrasov, S. Y.; Humphreys, C. J.; Sutton, A. P. Electron-energy-loss spectra and the structural stability of nickel oxide: An LSDA + *U* study. *Phys. Rev. B* **1998**, *57*, 1505–1509.

[27] Alexandrov, V.; Rosso, K. M. *Ab initio* modeling of Fe(II) adsorption and interfacial electron transfer at goethite (α-FeOOH) surfaces. *Phys. Chem. Chem. Phys.* **2015**, *17*, 14518–14531.

[28] Otte, K.; Schmahl, W. W.; Pentcheva, R. DFT + *U* study of arsenate adsorption on FeOOH surfaces: Evidence for competing binding mechanisms. *J. Phys. Chem. C* **2013**, *117*, 15571–15582.

[29] Otte, K.; Pentcheva, R.; Schmahl, W. W.; Rustad, J. R. Pressure-induced structural and electronic transitions in FeOOH from first principles. *Phys. Rev. B* **2009**, *80*, 205116.

[30] Monkhorst, H. J.; Pack, J. D. Special points for Brillouin-zone integrations. *Phys. Rev. B* **1976**, *13*, 5188–5192.

[31] Kresse, G.; Furthmüller, J. Efficiency of *ab initio* total energy calculations for metals and semiconductors using a plane-wave basis set. *Comput. Mater. Sci.* **1996**, *6*, 15–50.

[32] Momma, K.; Izumi, F. VESTA 3 for three-dimensional visualization of crystal, volumetric, and morphology data. *J. Appl. Crystallogr.* **2011**, *44*, 1272–1276.

[33] de la Fuente, D.; Alcántara, J.; Chico, B.; Díaz, I.; Jiménez, J. A.; Morcillo, M. Characterisation of rust surfaces formed on mild steel exposed to marine atmospheres using XRD and SEM/micro-Raman techniques. *Corros. Sci.* **2016**, *110*, 253–264.

[34] Das, S.; Hendry, M. J. Application of Raman spectroscopy to identify iron minerals commonly found in mine wastes. *Chem. Geol.* **2011**, *290*, 101–108.

[35] Fu, X. H.; Jia, L. C.; Wang, A. L.; Cao, H. J.; Ling, Z. C.; Liu, C. Q.; Shi, E. B.; Wu, Z. C.; Li, B.; Zhang, J. Thermal stability of akaganeite and its desiccation process under conditions relevant to Mars. *Icarus* **2020**, *336*, 113435.

[36] Xu, W.; Lan, H. C.; Wang, H. J.; Liu, H. M.; Qu, J. H. Comparing the adsorption behaviors of Cd, Cu, and Pb from water onto Fe-Mn binary oxide, MnO_2, and FeOOH. *Front. Environ. Sci. Eng.* **2015**, *9*, 385–393.

[37] Mohapatra, M.; Mohapatra, L.; Anand, S.; Mishra, B. K. One-pot synthesis of high surface area nano-akaganeite powder and its cation sorption behavior. *J. Chem. Eng. Data* **2010**, *55*, 1486–1491.

[38] Mishra, S.; Verma, N. Surface ion imprinting-mediated carbon nanofiber-grafted highly porous polymeric beads: Synthesis and application towards selective removal of aqueous Pb(II). *Chem. Eng. J.* **2017**, *313*, 1142–1151.

[39] Abdel-Samad, H.; Watson, P. R. An XPS study of the adsorption of lead on goethite (α-FeOOH). *Appl. Surf. Sci.* **1998**, *136*, 46–54.

[40] Gunneriusson, L.; Lövgren, L.; Sjöberg, S. Complexation of Pb(II) at the goethite (α-FeOOH)/water interface: The influence of chloride. *Geochim. Cosmochim. Acta* **1994**, *58*, 4973–4983.

[41] Sun, X. F.; Hu, C.; Hu, X. X.; Qu, J. H.; Yang, M. Characterization and adsorption performance of Zr-doped akaganéite for efficient arsenic removal. *J. Chem. Technol. Biotechnol.* **2013**, *88*, 629–635.

[42] Nieboer, E.; Fletcher, G. G.; Thomassen, Y. Relevance of reactivity determinants to exposure assessment and biological monitoring of the elements. *J. Environ. Monit.* **1999**, *1*, 1–14.

[43] Zhao, R.; Liu, J.; Gu, J. J. The effects of electrode thickness on the electrochemical and thermal characteristics of lithium ion battery. *Appl. Energy* **2015**, *139*, 220–229.

[44] Yue, J.; Jiang, X. C.; Yu, A. B. Experimental and theoretical study on the β-FeOOH nanorods: Growth and conversion. *J. Nanopart. Res.* **2011**, *13*, 3961–3974.

[45] Panayotova, M.; Velikov, B. Influence of zeolite transformation in a homoionic form on the removal of some heavy metal ions from wastewater. *J. Environ. Sci. Health A Tox. Hazard. Subst. Environ. Eng.* **2003**, *38*, 545–554.

[46] Xiong, C.; Wang, S. X.; Sun, W. T.; Li, Y. Selective adsorption of Pb(II) from aqueous solution using nanosilica functionalized with diethanolamine: Equilibrium, kinetic, and thermodynamic. *Microchem. J.* **2019**, *146*, 270–278.

[47] Chen, Y. B.; Tang, J. L.; Wang, S. X.; Zhang, L. B.; Sun, W. T. Bimetallic coordination polymer for highly selective removal of Pb(II): Activation energy, isosteric heat of adsorption, and adsorption mechanism. *Chem. Eng. J.* **2021**, *425*, 131474.

[48] Chakravarty, S.; Mohanty, A.; Sudha, T. N.; Upadhyay, A. K.; Konar, J.; Sircar, J. K.; Madhukar, A.; Gupta, K. K. Removal of Pb(II) ions from aqueous solution by adsorption using bael leaves (*Aegle marmelos*). *J. Hazard. Mater.* **2010**, *173*, 502–509.

[49] Sun, S. L.; Wang, L.; Wang, A. Q. Adsorption properties of crosslinked carboxymethyl-chitosan resin with Pb(II) as template ions. *J. Hazard. Mater.* **2006**, *136*, 930–937.